chemosensors

Article

Near-Infrared Molecular Photosensitizer Decorated with Quaternary Ammonium for High-Efficiency Photothermal Treatment of Bacterial Infections

Yuxuan He [1,2,†], Na Li [2,†], Sha Yang [2], Xiaofeng Tan [2], Li Tang [2,3] and Qinglai Yang [1,2,*]

[1] Department of Biochemistry and Molecular Biology, Hengyang Medica School, University of South China, Hengyang 421001, China
[2] Center for Molecular Imaging Probe, Hunan Province Key Laboratory of Tumor Cellular and Molecular Pathology, Cancer Research Institute, Hengyang Medical School, University of South China, Hengyang 421001, China
[3] Key Laboratory of Tropical Medicinal Plant Chemistry of Ministry of Education, College of Chemistry and Chemical Engineering, Hainan Normal University, Haikou 571158, China
* Correspondence: qingyu513@usc.edu.cn
† These authors contributed equally to this work.

Abstract: In recent years, pathogenic infections have been a growing health threat due to the proliferation of drug-resistant bacteria, so photothermal therapy (PTT) has gained considerable interest in biological and medical fields, owing to its noninvasive and highly effective properties. However, it is hard to achieve selective bacteria targeting while generating a large amount of heat at infected sites. Cationic electrostatic interaction is considered to be a common antimicrobial strategy. Herein, an organic molecule named **RT-MN** was synthesized with four positively charged quaternary ammonium salts that can bind to negatively charged bacteria. Under near-infrared 808 nm laser irradiation, **RT-MN** could be efficiently converted into a large amount of heat to eradicate bacteria. In addition, its good water solubility and biological safety proved that **RT-MN** has excellent biological application prospects. Overall, four such positively charged photosensitizer **RT-MN**, as a non-antibiotic treatment for resistant bacteria, could be promising for the exploration of highly effective antibacterial agents.

Keywords: antibacterial therapy; photothermal therapy (PTT); electrostatic interaction; quaternary ammonium

Citation: He, Y.; Li, N.; Yang, S.; Tan, X.; Tang, L.; Yang, Q. Near-Infrared Molecular Photosensitizer Decorated with Quaternary Ammonium for High-Efficiency Photothermal Treatment of Bacterial Infections. *Chemosensors* **2023**, *11*, 164. https://doi.org/10.3390/chemosensors11030164

Academic Editor: José M. Amigo

Received: 29 January 2023
Revised: 25 February 2023
Accepted: 27 February 2023
Published: 1 March 2023

1. Introduction

Antibiotics have been discovered for over seven decades and have saved countless lives. However, with the abuse and overuse of antibiotics worldwide, more and more resistant bacteria [1–4], such as *MRSA* and *VRE*, and even super bacteria, have emerged. The efficacy of traditional antibiotics has been limited, so there is an urgent need to develop new treatments that are capable of both avoiding bacterial resistance and killing bacteria efficiently. Recently, many new therapies that inhibit drug-resistant bacteria have emerged [5], such as antimicrobial nanomaterials [6–8], photothermal therapy (PTT) [9–16], photodynamic therapy (PDT) [17–19], photocatalytic therapy [20,21] and others.

Previous reports have demonstrated that PTT is more promising than traditional antibacterial methods, attributable to its noninvasive and high efficiency [22–24]. In the process of photothermal therapy, the photosensitizer generates considerable heat that is capable of destroying a cell membrane, denaturing proteins, inactivating enzymes and ultimately killing bacteria. Currently, there are many organic photothermal agents, mainly including porphyrin [25,26], indocyanine green [27,28], organic radical [29] and conjugated semiconductors [30], that have been applied in the antimicrobial field. However, there are many challenges associated with targeting bacteria selectively in an infected area while simultaneously producing a great deal of heat at the same time. In this study, we synthesized

a near-infrared molecular photosensitizer (**RT-MN**) modified with quaternary ammonium salts that selectively kill bacteria at high temperatures with irradiation of lasers of 808 nm (Scheme 1). A significant improvement in the labeling rate of bacteria was achieved using this strategy, which also solved the problem of bacterial drug resistance that is caused by conventional methods. In addition, according to bacterial plate count and live/dead staining tests in vitro, **RT-MN** killed more than 99% of bacteria with photothermal therapy. Under the irradiation of an 808 nm laser, **RT-MN** was also capable of effectively reducing the amount of inflammation in bacterially infected wounds as well as promoting the healing of these wounds; its good biocompatibility also proved that RT-MN has great potential for application in the future. This work draws a blueprint of electrostatic interaction to assist photothermal antibacterial treatment, which is expected to provide a new means for antibacterial treatment.

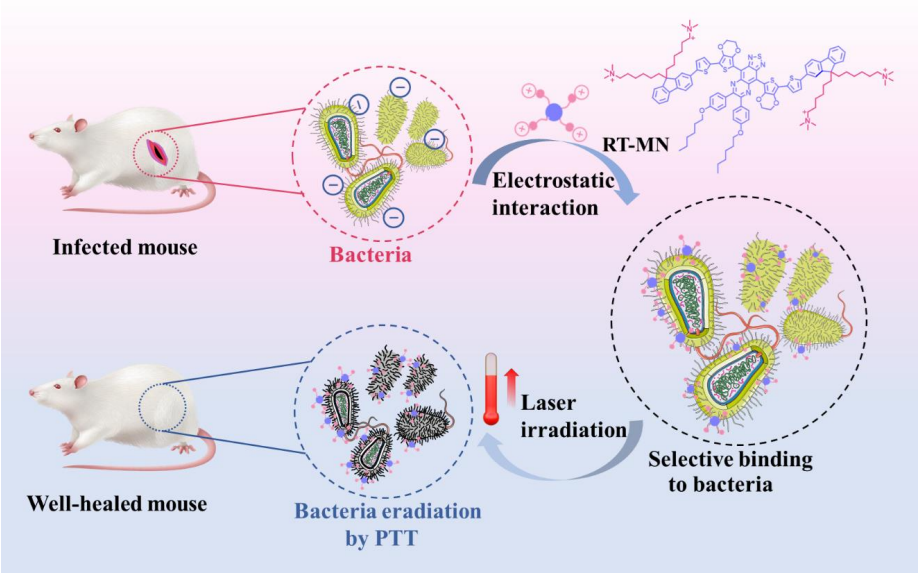

Scheme 1. Schematic illustration of near-infrared molecular photosensitizer **RT-MN** decorated with quaternary ammonium for high-efficiency photothermal treatment of bacterial infections.

2. Experimental Section

2.1. Reagents

The chemicals necessary for the experiment, including methyl tert-butyl ether (MTBE), dichloromethane, petroleum ether, tetrahydrofuran (THF), *N*,*N*-Dimethylformamide (DMF) and others for organic synthesis, were sourced from Shanghai Titan Scientific Co., Ltd. (Shanghai, China). They were used as is, without undergoing any further purification. The calcein-acetoxymethyl ester (calcein-AM)/Propidium iodide (PI) staining reagent was procured from Nanjing Vazyme BioTech Co. Ltd. (Nanjing, China). The *MRSA* (ATCC 43300), and *E. coli* (ATCC 1917) strains were obtained from the American Type Culture Collection (ATCC).

2.2. Apparatus

We used the Bruker AVANCE NEO 500 spectrometer to record ^{1}H NMR spectra and ^{13}C NMR spectra, using DMSO as the internal reference. We utilized the Thermo Scientific Q Exactive Combined Quadrupole-Orbitrap mass spectrometer in positive ion mode to obtain high-resolution mass spectra. The absorption spectra of UV-vis-NIR (ultraviolet, visible and near infrared) were measured using a spectrophotometer (MAPA-DA UV-3200S, Shanghai, China). We used a Fotric 225s infrared thermal imaging camera, equipped with an NIR laser, to monitor the temperature changes and thermal images of photothermal agents at a wavelength of 808 nm (MDL-XF-808, Changchun, China) with an intensity of 1.0 W·cm^{-2}. The confocal images were collected using a confocal laser scanning microscope

(Zeiss LSM980, Oberkochen, Germany). A nanometer particle size potentiometer (Malvern Panalytical Nano-ZS90, Malvern, UK) was utilized to measure the size and ζ potentials.

2.3. Synthesis of RT-MN

The specific synthesis route is shown in Figure 1, and the brief synthesis steps are as follows. Amounts of 6.0 g (24.4 mmol) of 2-bromofluorene **1**, 59.3 g (0.244 mol) of 1,6-dibromohexane **2** and 0.78 g (2.4 mmol) of tetrabutylammonium bromide were added to an aqueous solution of potassium hydroxide at 75 °C and cooled to room temperature after one hour of the reaction. After extraction, it was dried and recrystallized with petroleum ether at −20 °C to obtain product **3**. Compound **3** (5.71 g, 10.00 mmol) and compound **4** (5.60 g, 15.00 mmol) were dissolved in 100 mL of xylene, and $Pd(PPh_3)_4$ (1.16 g) was added under anaerobic conditions. The mixture was reacted at 130 °C for 5 h and then cooled to room temperature. After extraction and drying, product **5** was obtained through chromatography on a silica gel column. NBS (402 mg, 2.26 mmol) was dissolved in dichloromethane and then added dropwise to the dichloromethane solution of product **5**, and it reacted overnight in the dark and at room temperature. It was then purified with silica gel column chromatography to obtain product **6**. Compounds **6** (1.31 g, 2.00 mmol) and **7** (3.00 mmol) and $Pd(PPh_3)_4$ (231 mg, 0.20 mmol) were dissolved in 30 mL of xylene under oxygen-free conditions, reacted at 130 °C for 5 h and then cooled to room temperature. After extraction, it was dried, and compound **8** was obtained after chromatography with a silica gel column. THF (15 mL) was added to compound **8** (0.69 g, 1.50 mmol) at −78 °C nitrogen, followed by an *n*-BuLi solution (2.5 M hexane solution, 0.90 mL, 2.25 mmol). Tributyltin chloride (0.73 g, 2.25 mmol) was added two hours after the reaction. Then, the temperature was slowly raised to room temperature and reacted overnight. After extraction, crude product **9** was obtained after drying. In the absence of oxygen, compound **10** was dissolved in 20 mL of xylene with product **9**. Then, $Pd(PPh_3)_2Cl_2$ (70 mg, 0.1 mmol) was added and reacted at 130 °C for 10 h. After cooling to room temperature, it was extracted and dried, and finally, the chromatography yielded product **11**. DMF (5 mL), compound **11** (101 mg, 0.50 mmol) and trimethylamine dissolved in THF solution (118 mg, 2.00 mmol, 1.0 m, 2.0 mL) were reacted at 110 °C for 24 h. After cooling to room temperature, it was added to methyl tertiary butyl ether (MTBE), and then the heterogeneous mixture was separated via high-speed centrifugation. **RT-MN** was obtained after washing with MTBE. The ^{1}H NMR spectra and ^{13}C NMR spectra of intermediate products can be found in the supporting information (Figures S1–S10). The ^{1}H NMR spectra and ^{13}C NMR spectra of **RT-MN** can be found in the supporting information (Figures S11 and S12). The high-resolution mass spectra of **RT-MN** can be found in the supporting information (Figure S13).

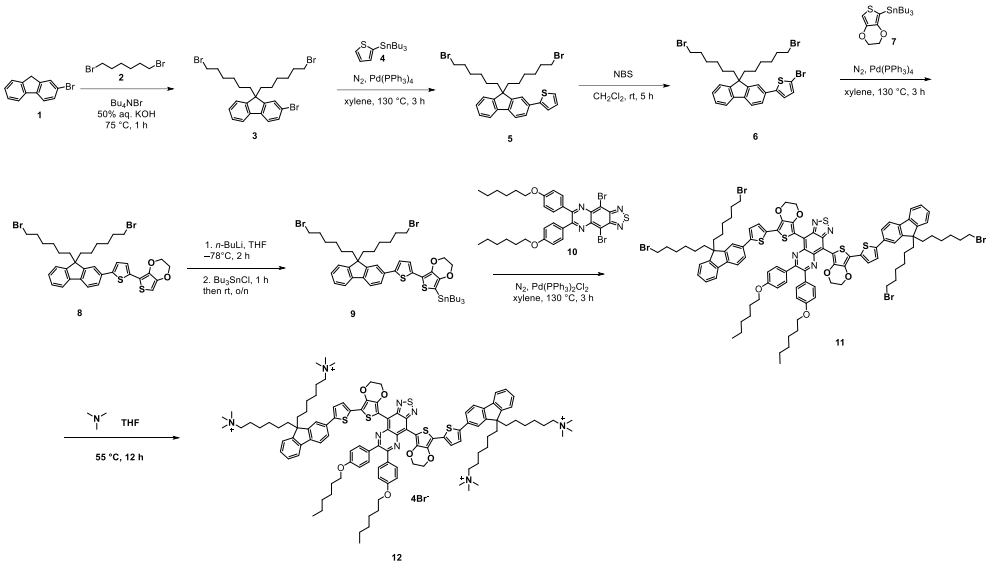

Figure 1. Synthesis route of **RT-MN**.

2.4. Photothermal Performance of RT-MN

In this part of the study, we aimed to evaluate the photothermal effect of **RT-MN** using an 808 nm laser. First, a 1.0 mL solution of **RT-MN** at various concentrations (0, 50, 100, 150, 200 and 250 μM) was irradiated for 10 min with the laser. The temperature change and thermal imaging were then captured using an infrared thermal imaging camera. Then, we examined the effects of different power densities (0.5, 0.75, 1.0, 1.25 and 1.5 W·cm^{-2}) on the photothermal effect of **RT-MN** (at a concentration of 150 μM). Finally, to determine the photothermal conversion efficiency (η), we used the reported [31] method and estimated it using Equations (1)–(5).

$$\eta = \frac{hs(T_{max} - T_{surr}) - Q_0}{I(1 - 10^{-A_{808}})} \quad (1)$$

The following equations can be used to calculate *hs*.

$$hs = \frac{cm}{\tau_s} \quad (2)$$

$$\tau_s = \frac{t}{-ln\theta} \quad (3)$$

$$\theta = \frac{T - T_{surr}}{T_{max} - T_{surr}} \quad (4)$$

$$Q_0 = hs(T_{max} - T_{surr)} \quad (5)$$

h represents the heat transfer coefficient, which measures the heat transfer rate through a material. *S* represents the surface area of the sample container, which can also affect the heat transfer rate. A larger surface area generally results in a faster heat transfer rate.

T_{max} represents the steady-state maximum temperature, the highest temperature reached during the cooling stage of the experiment. T_{surr} represents the ambient room temperature, which is the temperature of the environment surrounding the sample container. *T* represents the instantaneous temperature at this moment. *t* represents the time in the cooling stage, which is the amount of time that has passed since the start of the cooling stage. c represents the specific heat capacity of water, which measures the energy required to raise the temperature of a given mass of water by one degree Celsius. *m* represents the mass of the solution (g) used in the experiment. Q_0 represents the energy input by the same solvent without NPs (nanoparticles) after laser irradiation under the same conditions.

2.5. Antibacterial Assays In Vitro

Single bacteria colonies (*E. coli* and *MRSA*) were carefully selected and inoculated into 6–8 mL of LB liquid medium. The inoculated medium was then incubated in a shaking incubator at a temperature of 37 °C and a shaking speed of 120 rpm until the mid-log growth phase was reached (OD_{600} = 0.5). To prepare the bacterial suspensions for the different experimental groups, the bacterial concentration was adjusted to 10^7 CFU/mL, and the suspensions were incubated at 37 °C for 20 min. After incubation, the suspensions were either irradiated with an 808 nm near-infrared laser or left in the dark (1.0 W·cm^{-2}) for 10 min. To further assess the effect of the laser treatment, the bacterial suspension was sonicated for 2 min. Next, 100 mL of the diluted suspension of each group was uniformly applied to solid LB agar plates and incubated for 14–16 h at 37 °C. The bacterial survival rate was then calculated as follows: bacterial survival rate (%) = experimental group CFU/control group CFU × 100%, where the experimental group CFU and the control group CFU are the average CFUs of the experimental group and the control group, respectively. All experiments were repeated three times to ensure the accuracy and reliability of the results.

2.6. Live/Dead Staining

The experiment was conducted according to the instructions provided in the bacterial live/dead staining kit from BestBio company. The bacterial suspensions from the different

treatment groups were processed and incubated in the dark at 37 °C for 15 min. After the treatment with the dye, the bacterial suspensions were washed three times with sterile PBS buffer after being centrifuged at 3000 rpm for 5 min. Finally, the processed bacterial suspensions were added to a confocal dish for confocal microscopy imaging. The imaging was performed using two fluorescent channels: the PI red fluorescent channel with an excitation wavelength of 535 nm and emission wavelength of 630 nm, and the calcein-AM green fluorescent channel with an excitation wavelength of 488 nm and emission wavelength of 530 nm.

2.7. Evaluation of Antibacterial Activity In Vivo

In this study, we used female BALB/C mice that were 6–8 weeks old. An 8 mm wound was made on the left back of each mouse, and a bacterial suspension of *MRSA* (10^6 CFU/mL) was applied to the wound in order to create a bacterial infection. The mice with completed wounds were then divided into groups and treated every two days. The specific method used in this study was as follows. An amount of 100 μL of bacterial suspension (10^6 CFU/mL) was applied to the artificial wound on the back of the mouse. Twenty-four hours later, according to the grouping, 100 μL of different solutions (the first two groups were PBS, and the last two groups were 150 μM RT-MN water solution) were applied to the mouse wounds and then treated under 808 nm laser irradiation or in the dark for 10 min. During the treatment, representative thermal images of mice in different treatment groups exposed to the 808 nm laser (1.0 $W \cdot cm^{-2}$) for 10 min were collected using a thermal camera. The infected wounds were treated every two days according to the different groups for ten days. The wound diameter and weight of each group of mice were recorded throughout the treatment period to measure the effectiveness of the different treatments.

After the mice had undergone treatment, we sacrificed them and collected the entire wound and surrounding skin tissue. For each group, the whole wounds and surrounding skin tissues were sonicated in 2 mL of sterile PBS for 15 min, and the bacteria were resuspended in sterile PBS. After, 100 mL of the sonicated bacterial suspension was used to perform a routine bacteria-coated plate experiment. The number of colonies on these plates was used to evaluate the number of bacteria present in the infected tissue. To further evaluate the effectiveness of the different treatment methods, the infected skin tissue was cut off after treatment and fixed in a 4% polyformaldehyde solution. The samples were then embedded in paraffin and made into slices. These slices were then stained using the hematoxylin and eosin (H&E) method and Masson's staining method. This allowed us to examine the tissue samples under a microscope and observe any changes that occurred due to the treatment. Blood samples were also collected from the mice for routine blood analysis and a hemolysis test. This was performed to determine if there were any negative effects on the mice's blood due to the treatment. In addition, important organs such as the heart, liver, spleen, lung and kidney were collected for further analysis of biosafety. This was performed to ensure that the used treatment methods did not have any negative effects on the mice's overall health and well-being.

3. Results and Discussion

3.1. Evaluation of RT-MN Physicochemical Properties and Ability to Bind to Bacteria

Figure 2A presented the structure of RT-MN, and Figure 2B shows that **RT-MN** had a broad and distinct absorption peak between 600 nm and 900 nm, with a maximum value at 725 nm. In addition, under the irradiation of the 808 nm laser, the electron energy could be converted into heat energy.

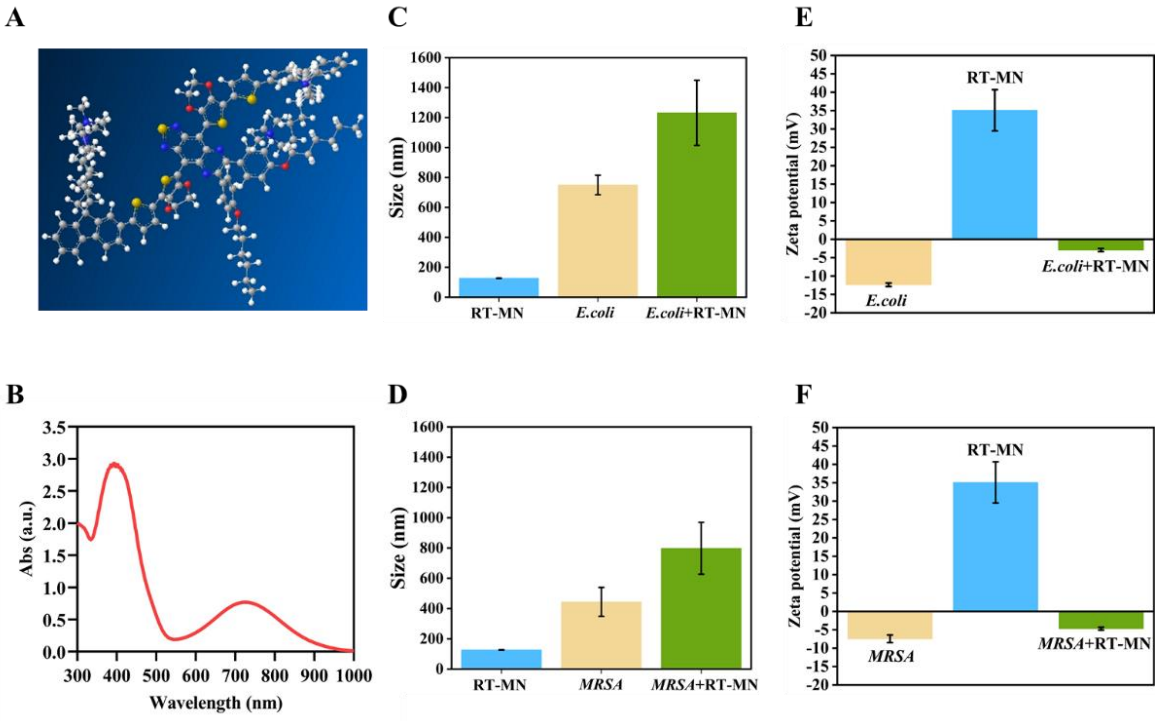

Figure 2. Characterizations of compounds. (**A**) Structure of **RT-MN**. (**B**) Absorbance of **RT-MN** aqueous solution. Particle size of **RT-MN** aqueous solution, particle size of (**C**) *E. coli* and (**D**) *MRSA* suspension, and particle size of both incubated together. ζ potential of **RT-MN** aqueous solution, ζ potential of (**E**) *E. coli* and (**F**) *MRSA* suspension, and potential of both incubated together.

Figure 2C,D present the results of the particle size measurements of **RT-MN** before and after incubation with bacteria. The data reveal that, after the incubation of **RT-MN** with bacteria, there was a significant increase in the particle size of **RT-MN**, which also strongly indicates that **RT-MN** could bind to bacteria. The nanoparticle size potentiometer revealed that RT-MN had a positive charge, whereas *MRSA* and *E. coli* were negatively charged. However, the ζ potential after the incubation of RT-MN and bacteria was between the bacteria and **RT-MN**, indicating that the binding ability of RT-MN to bacteria was due to the electrostatic interaction from an electrochemical perspective, as seen in Figure 2E,F.

The above results indicate that RT-MN is capable of binding to bacteria through electrostatic adsorption, making it a potential candidate for use as an antimicrobial agent.

3.2. Evaluation of RT-MN Photothermal Performance

Based on the excellent near-infrared absorption properties of **RT-MN**, the photothermal effect of the **RT-MN** aqueous solution was further explored.

We investigated the photothermal performance of RT-MN under 1.0 $W \cdot cm^{-2}$ 808 nm laser irradiation. Figure 3A,C present the experiment data, which were obtained by measuring the temperature changes in different concentrations of the **RT-MN** aqueous solution under 808 nm laser irradiation. The data reveal that, as the concentration of the **RT-MN** aqueous solution increased, the temperature also increased rapidly, which indicates that **RT-MN** has excellent photothermal performance. It therefore should absorb significant laser energy that can be converted to heat. However, when the concentration of **RT-MN** exceeded 150 μM, the temperature was no longer affected by increasing the concentration, demonstrating the photothermal performance of **RT-MN** saturated at a concentration of 150 μM. This suggests that, when the concentration of **RT-MN** is more than 150 μM, adding more **RT-MN** does not increase the amount of heat generated. Therefore, 150 μM is the optimal concentration for achieving the best photothermal performance of **RT-MN**.

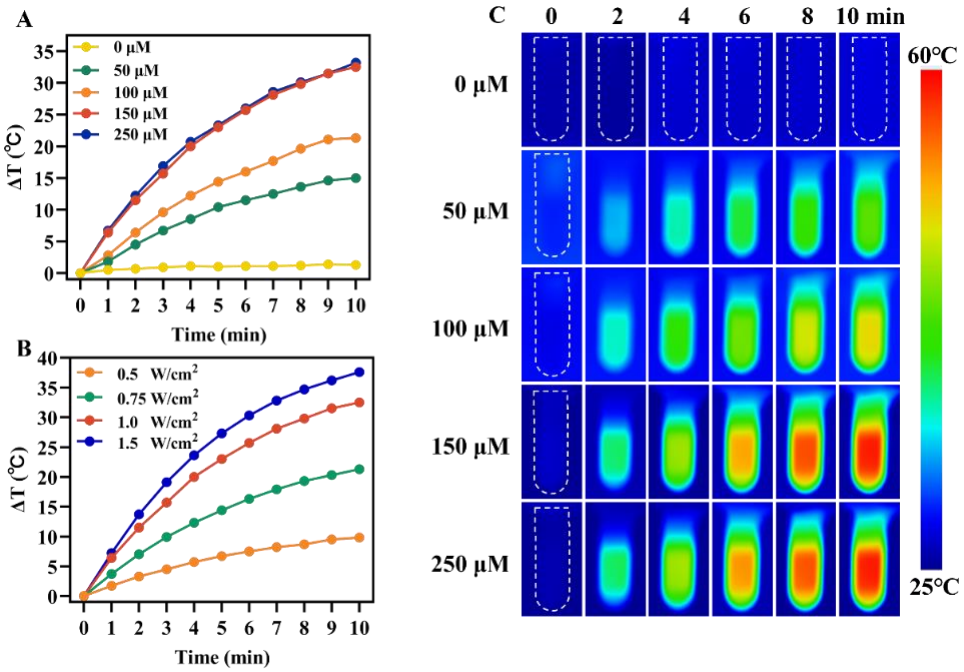

Figure 3. (**A**) Temperature change value of **RT-MN** aqueous solution with different concentrations for 10 min of laser irradiation (power density: 1.0 W·cm^{-2}). (**B**) Temperature change of **RT-MN** aqueous solution (150 μM) under different power densities of laser irradiation for 10 min. (**C**) Photothermal photos of each group under 808 nm laser (1.0 W·cm^{-2}) irradiation.

As shown in Figures 3B and S14, under the premise of an **RT-MN** concentration at 150 μM, temperature also increased rapidly with the power density. Moreover, when the laser power was 1.0 W·cm^{-2} and the concentration of **RT-MN** was 150 μM, the elevation was approximately 33 °C in 10 min and reached 60 °C, meeting the conditions required for the photothermal treatment of bacterial infections. The above results prove that **RT-MN** had excellent photothermal performance. The thermal conversion efficiency (η) of **RT-MN** was determined to be 51% through the plotted heating and cooling curves (Figure S15), far surpassing the previously reported commercial photothermal agent-IR820 [32], indicating that **RT-MN** has exceptional photothermal conversion ability and great photothermal treatment potential. These results confirm that **RT-MN** was an excellent photothermal agent and theoretically could meet the requirements for the photothermal treatment of bacterial infections.

3.3. Evaluation of RT-MN Antibacterial Effect In Vitro

The photothermal properties of **RT-MN** provided an excellent basis for further investigation of antimicrobial properties in vitro. Two representative strains of *E. coli* and *MRSA* were selected to verify the **RT-MN** antibacterial effect in vitro. Figure 4A presents the results of this experiment. The data show that, when the bacteria were exposed to 150 μM **RT-MN** and the 808 nm laser (at a power density of 1.0 W·cm^{-2} for 10 min), there was a significant reduction in the number of viable bacteria. Specifically, the results show that almost no bacteria colonies were visible after treatment with **RTMN** + NIR, which suggests that the **RT-MN** and laser combination can effectively inhibit the growth of *MRSA* and *E. coli*.

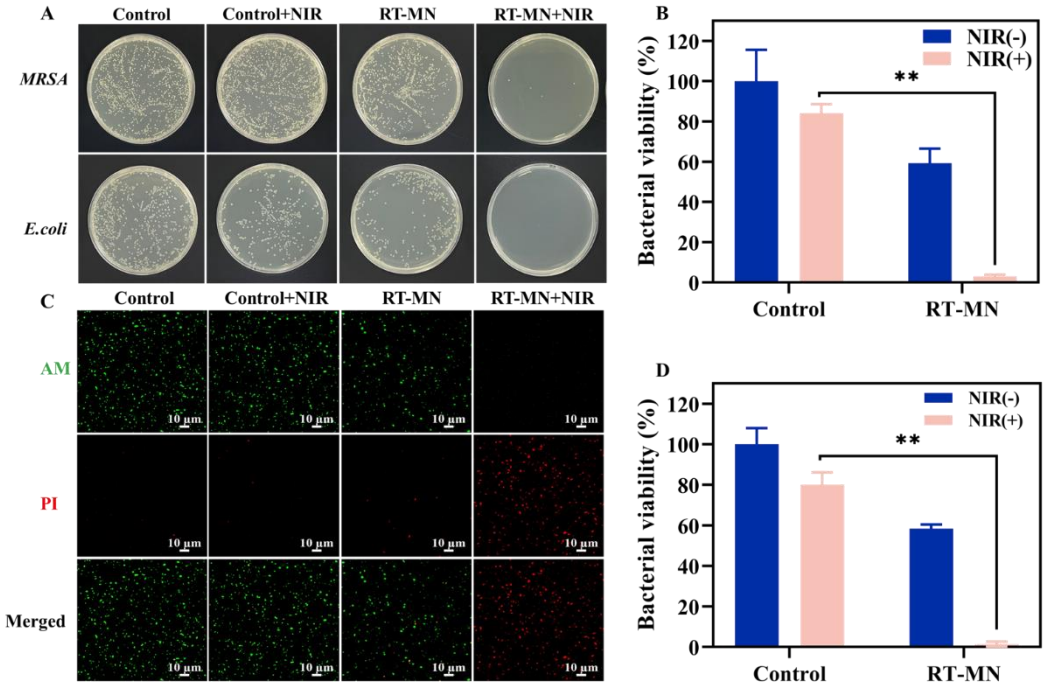

Figure 4. Antimicrobial effect of **RT-MN** in vitro: (**A**) Growth of colonies on the LB agar plate in different treatment groups (control, control + NIR, **RT-MN** and **RT-MN** + NIR). (**B**) Survival rate of (**B**) *MRSA* and (**D**) *E. coli* for different treatment groups. Error bars represent the standard deviation from the mean, and asterisks reflect statistically significant differences (** $p < 0.01$). (**C**) Live/dead staining image of *E. coli* treated in the different treatment groups.

Analyzing the data after evaluating the growth of the bacterial plates in different treatment groups revealed that the survival rate in the **RT-MN** + NIR group was only 1% (Figure 4B,D), whereas that of the **RT-MN** group was approximately 50%. This indicates that **RT-MN** could greatly enhance the bactericidal effect under 808 nm laser irradiation and that laser irradiation was a necessary factor for **RT-MN** to exert its bactericidal effect.

The live/dead staining assays were an effective tool for evaluating the antibacterial activity following different treatments with confocal laser scanning microscopy (CLSM). The dead *MRSA* and *E. coli* could be labeled with PI (red fluorescence), which could bind to the DNA by passing through the destroyed membrane of the cell [33]. The live/dead staining in Figure 4C displays that the red fluorescence (dead signal) was present in the entire field of vision, signifying that the *E. coli* treated with **RT-MN** + NIR were almost killed by PTT. These results confirm that **RT-MN** has the ability to kill bacteria efficiently via PTT.

3.4. Evaluation of Mouse Wound Models

Due to the unexpectedly high effectiveness of the in vitro antimicrobial experiment, we further extended the study to experiments in vivo. Figure 5A demonstrates the progress of infected wound healing in various treatment groups through visual representation. The data suggest that the treatment group that received **RT-MN** + NIR had the most rapid and efficient healing process. On the tenth day of treatment, the wound in this group had nearly disappeared, indicating that the **RT-MN** + NIR treatment was highly effective in promoting wound healing and reducing the visibility of the infected wound. In contrast, the other treatment groups did not show the same level of improvement, indicating that the **RT-MN** + NIR treatment may be superior in this specific context. The results of this study imply that the **RT-MN** + NIR treatment may be a promising option for treating infected wounds in the future.

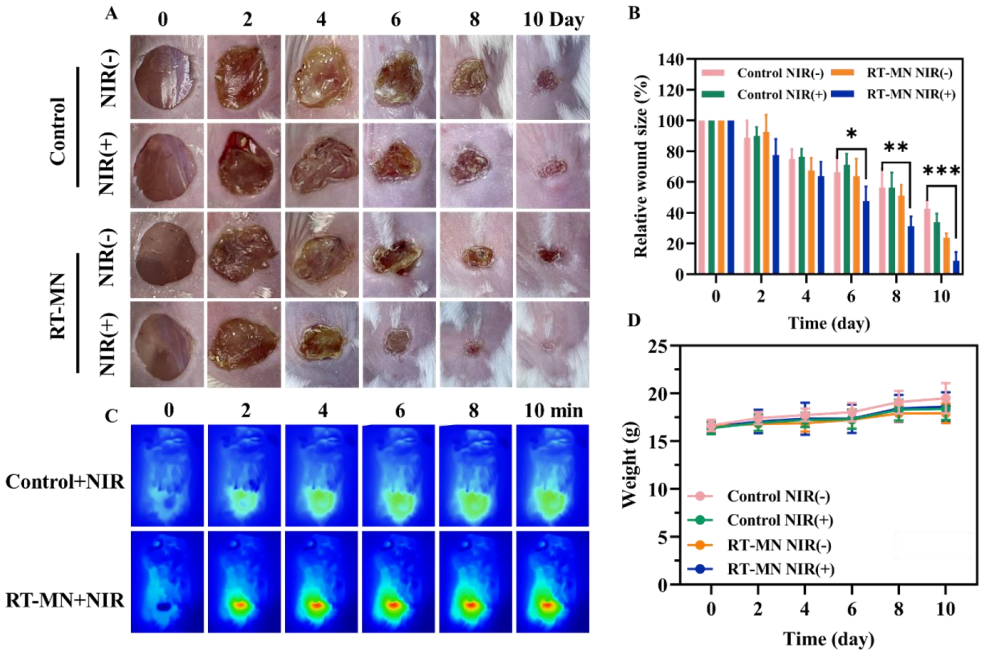

Figure 5. In vivo antibacterial evaluation of **RT-MN** on *MRSA*-infected wounds of mice: (**A**) Healing of wounds in mice in different groups. (**B**) Relative wound diameter in different groups. (**C**) Thermal infrared images were taken during the 10 min treatment. (**D**) Weight changes of mice. Asterisks reflect statistically significant differences (* $p < 0.05$, ** $p < 0.01$, *** $p < 0.001$).

Figure 5B provides a visual representation of the relative changes in the diameter of infected wounds among various treatment groups over time. This was accomplished by measuring the diameter of the wounds daily. The data indicate that the **RT-MN** + NIR group had a more significant reduction in wound diameter as compared to the other groups. This suggests that the **RT-MN** + NIR treatment may be particularly effective in reducing the sizes of infected wounds. This information can be used to compare the different treatment options' effectiveness and determine which may be the best for treating infected wounds.

When the mice with an artificially infected wound received laser treatment, thermal images were collected in infrared thermal camera photographs every two minutes, and the images showed the changes in temperature in the wounds and their surroundings during treatment after incubation with different treatments. As can be seen from Figure 5C, the wound temperature of the mice rose significantly after the **RT-MN** + NIR treatment and reached roughly 50 °C. The above results indicate that **RT-MN** could effectively treat bacterial infections in vivo with PTT, and it also accelerated infected wound healing at the same time.

We also evaluated the physiological impact of the different treatments on the mice by measuring and recording their body weight changes. Figure 5D presents the data for the body weight changes of all mice during the treatment period. The results show that there was almost no difference in body weight changes between the **RT-MN** + NIR and control groups during treatment, which suggests that the **RT-MN** + NIR treatment did not significantly negatively affect the mice's overall health and well-being.

3.5. Evaluation of RT-MN Biosafety

Furthermore, in order to ensure the safety of **RT-MN**, a series of additional tests were performed to evaluate its biosafety. One of the critical tests conducted was a routine blood analysis, which revealed that **RT-MN** had a very minimal impact on blood cells, such as platelets and monocytes. This suggests that **RT-MN** does not cause any significant damage to blood cells, making it a safe option for further use. Additionally, biochemical indices were measured to evaluate the liver and kidney functions of mice in all groups.

These tests' results indicate that the mice's liver and kidney functions remained normal, even after exposure to **RT-MN**. This further supports the conclusion that **RT-MN** is not harmful to the body and can be safely used in further studies. Overall, the results of these various biosafety tests provide strong evidence that **RT-MN** is a safe and viable option for further research and development. (In Figure 6A, the first row shows the biochemical indices; from left to right are aspartate aminotransferase (**AST**), alkaline phosphatase (**ALP**), alanine aminotransferase (**ALT**), creatinine (**CREA**) and blood urea nitrogen (**BUN**). The second and third rows are the results of the routine blood analysis; from left to right are the number of lymphocytes, red blood cells (**RBC**), white blood cells (**WBC**), neutrophils, platelets (**PLT**), monocytes, hemoglobin (**HGB**) content, mean corpuscular volume (**MCV**), red cell distribution width coefficient of variation (**RDW**) and mean corpuscular hemoglobin (**MCH**).)

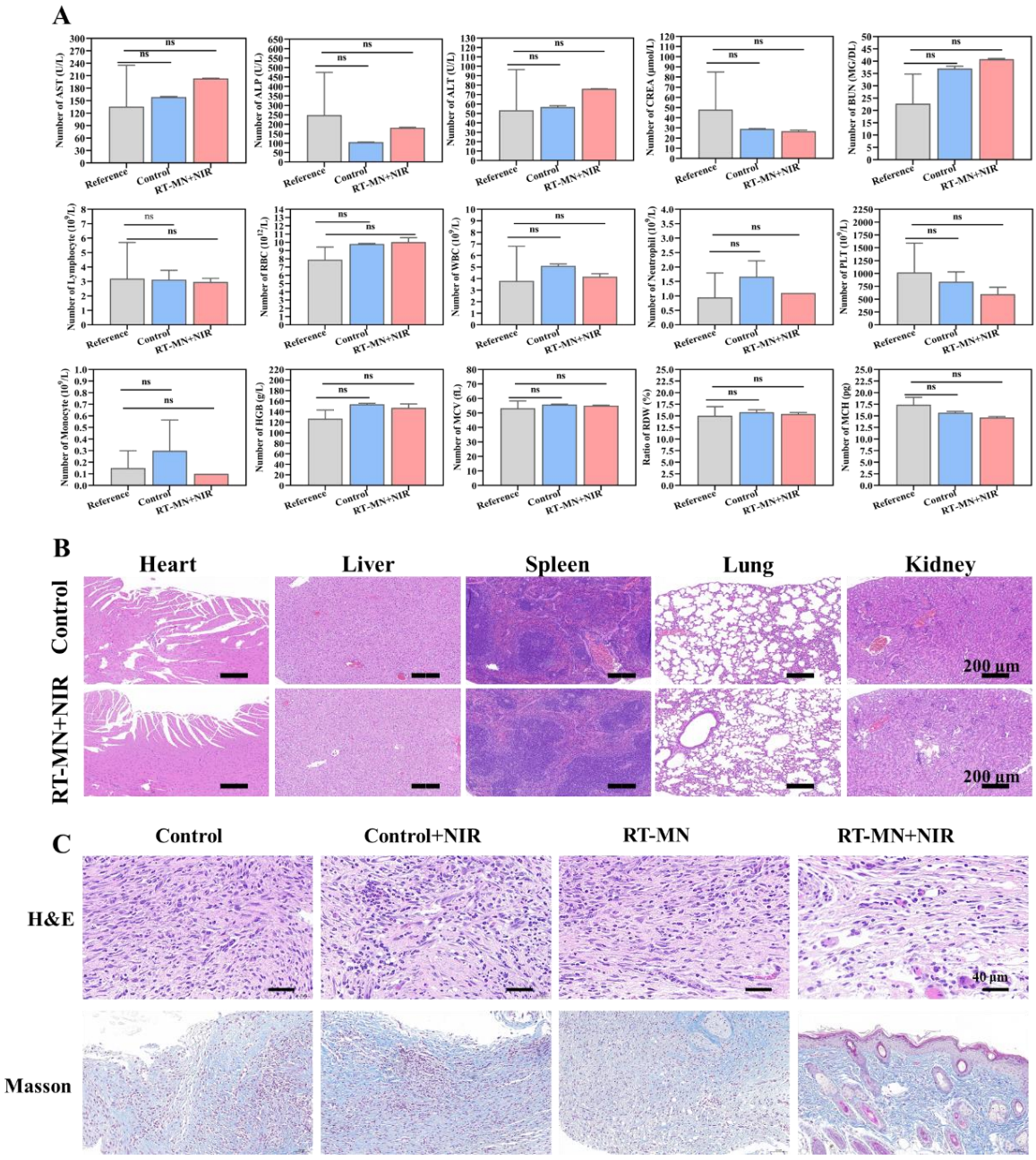

Figure 6. Evaluation of the biocompatibility of **RT-MN**: (**A**) Change in each index of group control and **RT-MN** + NIR. (**B**) Pathological sections of the heart, liver, spleen, lung and kidney. (**C**) H&E staining and Masson staining of wound skin sections of the control and the **RT-MN** + NIR groups.

As a second step in verifying the biosafety of **RT-MN**, tissue samples were collected from mice's hearts, livers, spleens, lungs and kidneys in both the **RT-MN** + NIR and control groups. These samples were then examined under a microscope to look for any pathological changes or abnormalities. The results of this analysis showed that there were no significant pathological changes observed in the tissue samples from either group. This suggests that **RT-MN** does not cause any harm to these vital organs and that it can be safely used without causing damage in vivo (Figure 6B).

In addition to the biosafety tests, further experiments were conducted to examine the wound-healing capability of **RT-MN**. One of the used methods was the examination of skin wounds stained with hematoxylin and eosin (H&E). This staining technique allows for the visualization of skin structures and can reveal any changes in the skin's inflammatory response. The results of this analysis show that the control group displayed a significant presence of inflammatory cells in the wound area. This suggests that the control group had a heightened inflammatory response, which could delay the healing process. In contrast, the **RT-MN** group displayed a lesser inflammatory response under laser irradiation (Figure 6C). Additionally, the staining results also show that there was more collagen fiber present in the wounds of the experimental group. Collagen is a protein that plays a crucial role in the wound healing process, as it helps to repair and strengthen damaged tissue. The presence of more collagen fibers in the wounds of the experimental group indicates that **RT-MN** may have a positive effect on collagen production, which can contribute to a better wound-healing effect (Figure 6C). Therefore, the above results indicate that **RT-MN** has good biocompatibility and the potential for clinical translation.

4. Conclusions

In summary, we synthesized a functionalized water-soluble photothermal agent (**RT-MN**) using the principle of electrostatic adsorption for photothermal antibacterial treatment. By using the mutual attraction of positive and negative charges, **RT-MN** molecules can be attached to the cell membranes of bacteria. More importantly, **RT-MN** has satisfactory photothermal properties due to the generation of a large amount of heat, which can be used to eradicate bacteria around it through PTT. Subsequently, the in vivo anti-infective ability of **RT-MN** was successfully demonstrated in an *MRSA*-infected mouse skin wound model. In addition to providing valuable practice for designing photothermal agents that specifically eliminate bacteria, this study holds promise for the use of next-generation antimicrobial agents in clinical applications.

Supplementary Materials: The following supporting information can be downloaded at https://www.mdpi.com/article/10.3390/chemosensors11030164/s1, Synthetic route of **RT-MN**; ^{1}H NMR, ^{13}C NMR and HRMS spectra of **RT-MN** (Figures S1–S13); Thermal infrared images of **RT-MN** under 808 nm laser irradiation with different power densities (Figure S14); Photothermal effect of **RT-MN** in water when irradiated with an 808 nm laser (Figure S15).

Author Contributions: Conceptualization, L.T. and Q.Y.; formal analysis, X.T., Y.H. and N.L.; investigation, Y.H., N.L. and S.Y.; data curation, Y.H. and N.L.; writing—review and editing, N.L., L.T. and Q.Y.; supervision, N.L., L.T. and Q.Y.; funding acquisition, L.T., X.T. and Q.Y. All authors have read and agreed to the published version of the manuscript.

Funding: Q.Y. acknowledges financial support from the National Science Foundation of China (81801749), the Science and Technology Innovation Program of Hunan Province "Huxiang Young Talents Plan" (2021RC3106) and the Key Research and Development Program of Hunan Province, China (no. 2022SK2053). L.T. thanks the Natural Science Foundation of Hunan Province of China (2022JJ40361) for funding. X.T. thanks the Natural Science Foundation of Hunan Province of China (2022JJ40360) for funding.

Institutional Review Board Statement: All animal experiments were approved by the University of South China Animal Experiment Ethics Review and the Health Guide for the Care and Use of Laboratory Animals of National Institutes. All mice received care in accordance with international ethics guidelines.

Informed Consent Statement: Not applicable.

Data Availability Statement: Not applicable.

Conflicts of Interest: The authors declare no conflict of interest.

References

1. Chambers, H.F.; DeLeo, F.R. Waves of resistance: Staphylococcus aureus in the antibiotic era. *Nat. Rev. Microbiol.* **2009**, *7*, 629–641. [CrossRef] [PubMed]
2. Gonzales, R.D.; Schreckenberger, P.C.; Graham, M.B.; Kelkar, S.; DenBesten, K.; Quinn, J.P. Infections due to vancomycin-resistant Enterococcus faecium resistant to linezolid. *Lancet* **2001**, *357*, 1179. [CrossRef] [PubMed]
3. Tacconelli, E.; Cataldo, M.A. Vancomycin-resistant enterococci (VRE): Transmission and control. *Int. J. Antimicrob. Agents* **2008**, *31*, 99–106. [CrossRef] [PubMed]
4. Liu, Y.-Y.; Wang, Y.; Walsh, T.R.; Yi, L.-X.; Zhang, R.; Spencer, J.; Doi, Y.; Tian, G.; Dong, B.; Huang, X.; et al. Emergence of plasmid-mediated colistin resistance mechanism MCR-1 in animals and human beings in China: A microbiological and molecular biological study. *Lancet Infect. Dis.* **2016**, *16*, 161–168. [CrossRef]
5. Xiao, Q.C.; Mai, B.J.; Nie, Y.C.; Yuan, C.; Xiang, M.H.; Shi, Z.H.; Wu, J.; Leung, W.N.; Xu, C.S.; Yao, S.Q.; et al. In Vitro and In Vivo Demonstration of Ultraefficient and Broad-Spectrum Antibacterial Agents for Photodynamic Antibacterial Chemotherapy. *ACS Appl. Mater. Interfaces* **2021**, *13*, 11588–11596. [CrossRef]
6. Wang, Y.; Zhao, Y.; Wu, J.; Li, M.; Tan, J.; Fu, W.; Tang, H.; Zhang, P. Negatively Charged Sulfur Quantum Dots for Treatment of Drug-Resistant Pathogenic Bacterial Infections. *Nano Lett.* **2021**, *21*, 9433–9441. [CrossRef]
7. Dong, B.; Li, C.; Chen, G.; Zhang, Y.; Zhang, Y.; Deng, M.; Wang, Q. Facile synthesis of highly photoluminescent Ag2Se quantum dots as a new fluorescent probe in the second near-infrared window for in vivo imaging. *Chem. Mater.* **2013**, *25*, 2503–2509. [CrossRef]
8. Luo, H.; Jiang, Y.-Z.; Tan, L. Positively-charged microcrystalline cellulose microparticles: Rapid killing effect on bacteria, trapping behavior and excellent elimination efficiency of biofilm matrix from water environment. *J. Hazard. Mater.* **2021**, *424*, 127299. [CrossRef]
9. Feng, T.; Lu, H.; Ye, X.; Nie, C.; Zhang, J.; Yu, L.; Jin, H.; Li, P.; Huang, W. Selective inactivation of Gram-positive bacteria in vitro and in vivo through metabolic labelling. *Sci. China Mater.* **2022**, *65*, 237–245. [CrossRef]
10. Wang, X.-M.; Huang, L.; Wang, Y.-J.; Xuan, L.; Li, W.-W.; Tian, L.-J. Highly efficient near-infrared photothermal antibacterial membrane with incorporated biogenic CuSe nanoparticles. *Chem. Eng. J.* **2020**, *405*, 126711. [CrossRef]
11. Fu, Q.R.; Ye, J.M.; Wang, J.J.; Liao, N.S.; Feng, H.J.; Su, L.C.; Ge, X.G.; Yang, H.H.; Song, J.B. NIR-II Photoacoustic Reporter for Biopsy-Free and Real-Time Assessment of Wilson's Disease. *Small* **2021**, *17*, e2008061. [CrossRef] [PubMed]
12. Feng, G.X.; Mai, C.K.; Zhan, R.Y.; Bazan, G.C.; Liu, B. Narrow band gap conjugated polyelectrolytes for photothermal killing of bacteria. *J. Mater. Chem. B* **2015**, *3*, 7340–7346. [CrossRef] [PubMed]
13. Zhang, C.; Wang, K.; Guo, X.; Tang, Y. A cationic conjugated polymer with high 808 nm NIR-triggered photothermal conversion for antibacterial treatment. *J. Mater. Chem. C* **2021**, *10*, 2600–2607. [CrossRef]
14. Liu, Y.-S.; Wei, X.; Zhao, X.; Chen, L.-J.; Yan, X.-P. Near-Infrared Photothermal/Photodynamic-in-One Agents Integrated with a Guanidinium-Based Covalent Organic Framework for Intelligent Targeted Imaging-Guided Precision Chemo/PTT/PDT Sterilization. *ACS Appl. Mater. Interfaces* **2021**, *13*, 27895–27903. [CrossRef] [PubMed]
15. Ye, Y.; He, J.; Qiao, Y.; Qi, Y.; Zhang, H.; Santos, H.A.; Zhong, D.; Li, W.; Hua, S.; Wang, W.; et al. Mild temperature photothermal assisted anti-bacterial and anti-inflammatory nanosystem for synergistic treatment of post-cataract surgery endophthalmitis. *Theranostics* **2020**, *10*, 8541–8557. [CrossRef]
16. Qian, W.; Yan, C.; He, D.F.; Yu, X.Z.; Yuan, L.; Liu, M.L.; Luo, G.X.; Deng, J. pH-triggered charge-reversible of glycol chitosan conjugated carboxyl graphene for enhancing photothermal ablation of focal infection. *Acta Biomater.* **2018**, *69*, 256–264. [CrossRef] [PubMed]
17. He, X.; Yang, Y.; Guo, Y.; Lu, S.; Du, Y.; Li, J.-J.; Zhang, X.; Leung, N.L.C.; Zhao, Z.; Niu, G.; et al. Phage-Guided Targeting, Discriminative Imaging, and Synergistic Killing of Bacteria by AIE Bioconjugates. *J. Am. Chem. Soc.* **2020**, *142*, 3959–3969. [CrossRef]
18. Xu, B.; Wang, H.; Wang, W.; Gao, L.; Li, S.; Pan, X.; Wang, H.; Yang, H.; Meng, X.; Wu, Q.; et al. A Single-Atom Nanozyme for Wound Disinfection Applications. *Angew. Chem. Int. Ed.* **2019**, *58*, 4911–4916. [CrossRef]
19. Shi, X.; Sung, S.H.P.; Chau, J.H.C.; Li, Y.; Liu, Z.; Kwok, R.T.K.; Liu, J.; Xiao, P.; Zhang, J.; Liu, B.; et al. Killing G(+) or G(−) Bacteria? The Important Role of Molecular Charge in AIE-Active Photosensitizers. *Small Methods* **2020**, *4*, 2000046. [CrossRef]
20. Zhang, C.P.; Guo, J.N.; Zou, X.Y.; Guo, S.Y.; Guo, Y.; Shi, R.W.; Yan, F. Acridine-Based Covalent Organic Framework Photosensitizer with Broad-Spectrum Light Absorption for Antibacterial Photocatalytic Therapy. *Adv. Healthc. Mater.* **2021**, *10*, e2100775. [CrossRef]
21. Wang, L.W.; Zhang, X.; Yu, X.; Gao, E.N.; Shen, Z.Y.; Zhang, X.L.; Ge, S.G.; Liu, J.; Gu, Z.J.; Chen, C.Y. An All-Organic Semiconductor C3N4/PDINH Heterostructure with Advanced Antibacterial Photocatalytic Therapy Activity. *Adv. Mater.* **2019**, *31*, e1901965. [CrossRef] [PubMed]

22. Li, Y.; Liu, F.; Zhang, J.; Liu, X.; Xiao, P.; Bai, H.; Chen, S.; Wang, D.; Sung, S.H.P.; Kwok, R.T.K.; et al. Efficient Killing of Multidrug-Resistant Internalized Bacteria by AIEgens In Vivo. *Adv. Sci.* **2021**, *8*, 2001750. [CrossRef]
23. Li, M.; Wen, H.; Li, H.; Yan, Z.-C.; Li, Y.; Wang, L.; Wang, D.; Tang, B.Z. AIEgen-loaded nanofibrous membrane as photodynamic/photothermal antimicrobial surface for sunlight-triggered bioprotection. *Biomaterials* **2021**, *276*, 121007. [CrossRef] [PubMed]
24. Wang, H.; Zhou, S.; Guo, L.; Wang, Y.; Feng, L. Intelligent Hybrid Hydrogels for Rapid In Situ Detection and Photothermal Therapy of Bacterial Infection. *ACS Appl. Mater. Interfaces* **2020**, *12*, 39685–39694. [CrossRef] [PubMed]
25. Zou, Q.; Abbas, M.; Zhao, L.; Li, S.; Shen, G.; Yan, X. Biological Photothermal Nanodots Based on Self-Assembly of Peptide–Porphyrin Conjugates for Antitumor Therapy. *J. Am. Chem. Soc.* **2017**, *139*, 1921–1927. [CrossRef] [PubMed]
26. Sun, Y.; Zhang, Y.; Gao, Y.; Wang, P.; He, G.; Blum, N.T.; Lin, J.; Liu, Q.; Wang, X.; Huang, P. Six Birds with One Stone: Versatile Nanoporphyrin for Single-Laser-Triggered Synergistic Phototheranostics and Robust Immune Activation. *Adv. Mater.* **2020**, *32*, e2004481. [CrossRef] [PubMed]
27. Lv, R.; Wang, D.; Xiao, L.; Chen, G.; Xia, J.; Prasad, P.N. Stable ICG-loaded upconversion nanoparticles: Silica core/shell theranostic nanoplatform for dual-modal upconversion and photoacoustic imaging together with photothermal therapy. *Sci. Rep.* **2017**, *7*, 15753. [CrossRef]
28. Sheng, Z.; Hu, D.; Zheng, M.; Zhao, P.; Liu, H.; Gao, D.; Gong, P.; Gao, G.; Zhang, P.; Ma, Y.; et al. Smart human serum albumin-indocyanine green nanoparticles generated by programmed assembly for dual-modal imaging-guided cancer synergistic phototherapy. *ACS Nano* **2014**, *8*, 12310–12322. [CrossRef]
29. Tang, B.; Li, W.; Chang, Y.; Yuan, B.; Wu, Y.; Zhang, M.; Xu, J.; Li, J.; Zhang, X. A Supramolecular Radical Dimer: High-Efficiency NIR-II Photothermal Conversion and Therapy. *Angew. Chem. Int. Ed.* **2019**, *58*, 15526–15531. [CrossRef]
30. Zhou, L.; Lv, F.; Liu, L.; Wang, S. Water-Soluble Conjugated Organic Molecules as Optical and Electrochemical Materials for Interdisciplinary Biological Applications. *Acc. Chem. Res.* **2019**, *52*, 3211–3222. [CrossRef]
31. Li, X.; Liu, L.; Li, S.; Wan, Y.; Chen, J.-X.; Tian, S.; Huang, Z.; Xiao, Y.; Cui, X.; Xiang, C.; et al. Biodegradable π-Conjugated Oligomer Nanoparticles with High Photothermal Conversion Efficiency for Cancer Theranostics. *ACS Nano* **2019**, *13*, 12901–12911. [CrossRef] [PubMed]
32. Zhang, D.; Zhang, J.; Li, Q.; Tian, H.; Zhang, N.; Li, Z.; Luan, Y. pH- and Enzyme-Sensitive IR820–Paclitaxel Conjugate Self-Assembled Nanovehicles for Near-Infrared Fluorescence Imaging-Guided Chemo–Photothermal Therapy. *ACS Appl. Mater. Interfaces* **2018**, *10*, 30092–30102. [CrossRef] [PubMed]
33. Xu, H.; Fang, Z.; Tian, W.; Wang, Y.; Ye, Q.; Zhang, L.; Cai, J. Green Fabrication of Amphiphilic Quaternized β-Chitin Derivatives with Excellent Biocompatibility and Antibacterial Activities for Wound Healing. *Adv. Mater.* **2018**, *30*, e1801100. [CrossRef] [PubMed]